IEEE Access
Multidisciplinary | Rapid Review | Open Access Journal

Received December 5, 2019, accepted December 22, 2019, date of publication December 30, 2019,
date of current version January 14, 2020.

Digital Object Identifier 10.1109/ACCESS.2019.2963042

Multi-Scene Deception Jamming on SAR Imaging With FDA Antenna

HUI WANG[1], SHUNSHENG ZHANG[1], WEN-QIN WANG[2], (Senior Member, IEEE), BANG HUANG[2], (Student Member, IEEE), ZHI ZHENG[2], (Member, IEEE), AND ZHENG LU[3], (Senior Member, IEEE)

[1]Research Institute of Electronic Science and Technology, University of Electronic Science and Technology of China, Chengdu 611731, China
[2]School of Information and Communication Engineering, University of Electronic Science and Technology of China, Chengdu 611731, China
[3]Beijing Institute of Spacecraft System Engineering, Beijing 100094, China

Corresponding author: Shunsheng Zhang (zhangss@uestc.edu.cn)

This work was supported in part by the National Natural Science Foundation of China under Grant 61671122 and 61571081.

ABSTRACT Most of the existing deception jamming techniques focus on designing effective jamming signals for static targets or scenes. This paper proposes a multi-scene deception jamming against synthetic aperture radar (SAR) imaging with frequency diverse array (FDA) antenna. Different from traditional single-element and phased-array antennas, FDA antenna employs a small frequency offset across the array elements to produce angle-, range- and even time-dependent transmit beampattern, which brings bright prospect for the application of new jamming techniques against SAR imaging. Such a new method will generate many false targets or multiple deception scenes for the jammed SAR, which helps jam better on the static scene and moving target. Moreover, the location and number of false targets can be manipulated. This paper will illustrate the FDA-based deception jamming against SAR imaging, specially designed waveform and the relationship between the number of false targets or scenes and FDA parameters. The relationship between the location of false targets and the position of jammer will also be described in detail. All proposed methods are validated by extensive simulation results.

INDEX TERMS Synthetic aperture radar (SAR), frequency diverse array (FDA), frequency offset, multi-scene deception jamming, manipulation.

I. INTRODUCTION

Along with the fast development of synthetic aperture radar (SAR) imaging technology [1], [2], it is increasingly necessary to apply this technology into jamming against unfriendly SAR imaging. In order to conceal some important targets and scenes, effective interference in the enemy's SAR must be implemented [3], [4].

Generally, SAR jamming techniques can be divided into passive [5]–[7] and active ones [8]–[10]. Passive jamming has the advantages of strong adaptability and easy production while the disadvantage is that the electromagnetic characteristics are not flexible and difficult to change according to the actual situation. The existing active jamming methods against SAR imaging usually emit noisy signals to cover a certain frequency band, which aims to protect the true targets [8]–[10]. However, a much higher transmit power is required for the jammer due to the fact that a high signal-to-noise ratio (SNR) gain can be achieved in the matched filtering of the unfriendly SAR [11], [12]. Deception jamming discussed in this paper [13]–[16], which makes the unfriendly SAR generate false targets or deceptive scenes in the final imaging requires much lower transmit power than the noise-jamming scheme. Therefore, more and more researchers pay more attention to deception jamming. Several typical deceptive jamming methods have been published, such as inverse range Doppler algorithm [16], segmented modulation [17] and premodulation [18], but they need a reconnaissance system to measure the parameters of the SAR to be jammed at first and are required to provide fast calculation strategies to improve the efficiency of the jamming signal generation. Although the jamming methods proposed in [19] can produce deceptive interference on SAR imaging, and the methods based on 1-bit sampling and time-varying thresholds proposed in [20] can conceal the true target on SAR imaging, multiple false scenes cannot be

The associate editor coordinating the review of this manuscript and approving it for publication was Hasan S. Mir.

generated simultaneously. The deception jamming methods proposed in [17], [21], [22], can generate false targets with high fidelity, but they require multiple receivers to work together, which will increase hardware costs and system complexity. Although this paper [23] mentions that the method can produce multiple false target interference, it needs to strictly control the delay time and sample length. [19]–[28] proposed its own deception jamming techniques for different scenarios of static scenes or moving targets.

Antenna plays an important role in various jamming techniques, but phased-array antenna only produces angle-dependent transmit beampattern. This paper, however, adopts frequency diverse array (FDA) antenna for deception jamming on SAR imaging [29]–[31]. Different from phased arrays, FDA uses a small frequency offset, as compared to the carrier frequency, across its array elements to produce angle-, range- and time-dependent transmit beampattern [32], [33]. These characteristics unlock the potential to develop new deceptive jamming approaches against SAR imaging. Compared with the linear frequency modulated (LFM) waveforms [26], the frequency offset can control the position of the false point target or scenes and control the appearance and disappearance of the false point target or scenes. The study of FDA interference was first mentioned in the 2018 IGARSS conference paper [34] and expand further by [35]. We should note that this paper is the extension of [34].

This paper proposes an efficient multi-scene deceptive jamming method against high-resolution synthetic aperture radar imaging. Such a method can make full use of the unique angle-, range- and time-independent FDA transmit beampattern and easily control the number of false targets or scenes and their locations. The number of false targets or scenes is determined by the number of FDA elements, and the ranges between false targets can be freely designed by controlling the FDA frequency offsets. Compared with traditional deceptive jamming techniques, the proposed deceptive jamming method is more efficient and reduces the requirements for the reconnaissance measurements. More importantly, the number and range of generated false targets or scenes can be easily controlled. This method works not only to static scenes and targets, but also to the moving targets without changing the jammer. Moreover, due to the innate range-, angle- correlation of the beam of FDA, the enemy cannot find the location of FDA jammer through the traditional angle measurement technology, which greatly improves the safety of jammer.

The rest sections of this paper are organized as follows: Section II introduces briefly the basics of deceptive jamming against high-resolution SAR imaging and formulates the motivation of this work. Section III discusses how FDA is employed in deceptive jamming against high-resolution SAR imaging. The next section presents the deceptive image formulation based on range-Doppler algorithm, together with imaging simulation results. Furthermore, the deceptive jamming performance is extensively evaluated in Section V. Finally, the conclusion and future work are drawn in Section VI.

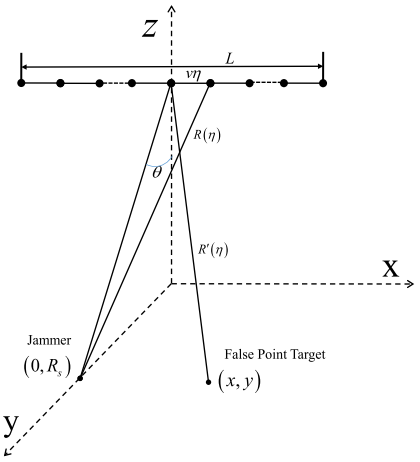

FIGURE 1. Geometric model for SAR deceptive jamming.

II. FOUNDATION AND MOTIVATION OF DECEPTION JAMMING

This section first introduces the geometric model for SAR deception jamming and deduces the instantaneous slant range of a false jamming point target. Then, the FDA antenna model is described in detail, which is the basis of deception jamming and the motivation of this research.

A. GEOMETRIC MODEL OF DECEPTIVE JAMMING AGAINST SAR IMAGING

The geometric relationship between the side-looking SAR and the jammer is shown in Fig. 1, where L is the synthetic aperture length and θ is the look-down angle. The SAR platform flies along an ideal straight line (x-axis) at an altitude h with a constant velocity v. The jammer is located at $(0, R_s)$, where R_s is determined by

$$R_s = h \cdot \tan\theta. \tag{1}$$

Suppose the beam center to the jammer at slow time $\eta = 0$. The instantaneous SAR-to-jammer range and SAR-to-false target range at the azimuth time η can be expressed, respectively, as

$$2R(\eta) = \sqrt{R_s^2 + h^2 + (v\eta)^2} \tag{2}$$

$$R'(\eta) = \sqrt{(R_s + y)^2 + h^2 + (x - v\eta)^2}. \tag{3}$$

where the coordinates (x, y) of the false point target are offsets from the jammer position (0, Rs). Since $(-L/(2v)) \leq \eta \leq (L/(2v))$, $R(\eta)$ and $R'(\eta)$ can be approximated by (see Appendix for the Taylor Expansion)

$$2R(\eta) \approx R_s + \frac{h^2}{2R_s} + \frac{(v\eta)^2}{2R_c} \tag{4}$$

$$\begin{aligned} R'(\eta) &\approx R_s + y + \frac{h^2}{2R_s} + \frac{x^2 + (v\eta)^2 - 2xv\eta}{2R_c} \\ &\approx R(\eta) + \Delta R(\eta) \end{aligned} \tag{5}$$

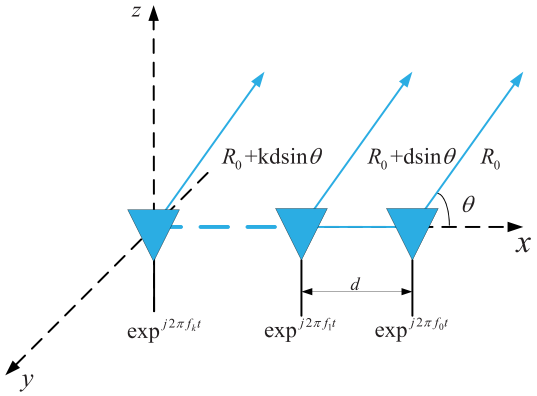

FIGURE 2. Geometry model of FDA transmitting signal.

where $R_c = \sqrt{R_s^2 + h^2}$ is the center slant range, and $\Delta R(\eta) = y + x^2/(2R_c) - xv\eta/R_c$ is the equivalent delay of the false point target relative to the jammer.

B. FDA SIGNAL MODEL

For simplicity and without loss of generality, we assume a uniform linear array containing M elements with spacing d, the frequency of the waveform radiated from each element is increased by a small frequency offset Δf, as shown in Fig. 2. Suppose each array element emits a linear-frequency-modulated (LFM) signal. That is, the signal radiated by the kth element is

$$s_k(t) = \text{rect}\left(\frac{t}{\tau}\right)\exp(j2\pi f_k t)\exp\left(j\pi K_r t^2\right) \tag{6}$$

where $rect\left(\frac{t}{\tau}\right) = \begin{cases} 1, for \left|\frac{t}{\tau}\right| \le \frac{1}{2} \\ 0, for \left|\frac{t}{\tau}\right| \ge \frac{1}{2} \end{cases}$, τ is the pulse duration, $K_r = \frac{B_r}{\tau}$ is the chirp rate, and B_r is the signal bandwidth. The overall carrier frequency of the kth element is $f_k = f_0 + (k-1)\Delta f, k = 0, 1, \cdots, M-1$, with f_0 as the carrier frequency for the first element.

Given a far-field point target P at the angle θ and range R_0, the total electric field can be expressed as

$$\begin{aligned} s(t, R_0, \theta) &= \sum_{k=0}^{M-1} s_k(t - \frac{R_k}{c}) \\ &= rect\left(\frac{t - \frac{R_k}{c}}{\tau}\right)\sum_{k=0}^{M-1}\frac{1}{R_k}\exp\{j(\omega_0 + \omega_k)\} \end{aligned} \tag{7}$$

where R_0 is the range from the first array element to the point target P. c is the speed of light. $\omega_0 = 2\pi\left\{f_0 t - \frac{R_0}{\lambda_0} + \frac{1}{2}K_r\left(t - \frac{R_k}{c}\right)^2\right\}$. $\omega_k = 2\pi\left(k\Delta f t - k\frac{\Delta f R_0}{c} - k\frac{d\sin\theta}{\lambda_0} - k^2\frac{\Delta f d\sin\theta}{c}\right)$, with $\lambda_0 = c/f_0$, $R_k = R_0 + kd\sin\theta$. Because of $R_k \approx R_0$ and $k^2\Delta f d\sin\theta/c \ll \pi/12$, equation (7) can be approximated as equation (8), as shown at the bottom of this page, where ϕ is expressed in equation (9), as shown at the bottom of this page.

The most striking feature of FDA is the small frequency offset that not only produces angle-, range- and time-dependent beampattern, but also can be used to develop new deceptive jamming methods against SAR imaging. This is just the motivation of this research.

III. FDA-BASED LARGE SCENE DECEPTIVE JAMMING METHOD

For the sake of simplicity, according to Fig. 1, we assume that the jammer is in the center of the imaging scene, and that its backscattering coefficient is set to 1, its echoes of jammer after carrier frequency removal can then be written as

$$\begin{aligned} s(t, \eta) = &\sum_{k=0}^{M-1} A_0\omega_r(t - 2R(\eta)/c)\,\omega_a(\eta - \eta_c) \\ &\times \exp\{-j4\pi f_k R(\eta)/c\}\exp(j2\pi k\Delta f t) \\ &\times \exp\left\{j\pi K_r(t - 2R(\eta)/c)^2\right\} \end{aligned} \tag{10}$$

where $\omega_r(\tau)$ and $\omega_a(\eta)$ denote the range and azimuth envelopes respectively, and η_c is the Doppler center time.

For the purpose of deceptive interference, the instantaneous slant range of the target with the false interference generated by the jammer must be approximately equal to that at the true point (x, y). Since the slant range of target point in the SAR to the scene is different, the delay amount of the target point echo signals is also different. According to equation 5, the returned signals of the false point targets can be obtained by delaying the signal intercepted by the jammer. The echoes of the false point target located at (x, y) can be expressed as

$$\begin{aligned} s'(t, \eta) = &A\exp\left(-\frac{j4\pi\Delta R(\eta)}{\lambda_0}\right)s(t, \eta) \\ &\otimes\sigma(x, y)\,\delta\left(t - \frac{2\Delta R(\eta)}{c}\right) \end{aligned} \tag{11}$$

$$\begin{aligned} s(t, R_0, \theta) &\approx rect\left(\frac{t - \frac{R_0}{c}}{\tau}\right)\frac{1}{R_0}\exp(j\varphi_0)\sum_{k=0}^{M-1}\exp\left\{j2\pi k\left(\Delta f t - \frac{\Delta f R_0}{c} - \frac{d\sin\theta}{\lambda_0}\right)\right\} \\ &\approx rect\left(\frac{t - \frac{R_0}{c}}{\tau}\right)\frac{\exp(j\phi)}{R_0}\frac{\sin\left[\pi M\left(\Delta f t - \frac{\Delta f R_0}{c} - \frac{d\sin\theta}{\lambda_0}\right)\right]}{\sin\left[\pi\left(\Delta f t - \frac{\Delta f R_0}{c} - \frac{d\sin\theta}{\lambda_0}\right)\right]} \end{aligned} \tag{8}$$

where

$$\phi = 2\pi\left\{f_0\left(t - \frac{R_0}{c}\right) + \frac{1}{2}K_r\left(t - \frac{R_0}{c}\right)^2 + \pi(M-1)\left(\Delta f t - \frac{\Delta f R_0}{c} - \frac{d\sin\theta}{\lambda_0}\right)\right\} \tag{9}$$

where $\otimes$ is the convolution operator. A is the jammer gain factor depending on the intensity of the jamming scene and the real scene around it, while $\sigma(x, y)$ represents the backscattering coefficient of the false point target in the scene. The echoes of the false scene can be regarded as the delay of the point target with respect to the echo of the jammer.

In order to enhance the speed and accuracy of false echo signal generation, the time domain convolution is usually accomplished by multiplying a linear phase factor in the frequency domain with an FFT transform. Applying Fourier transform to equation (11) with respect to the fast time, we can get the frequency-domain expression, as shown in equation (III). It is noticed that Part I only relies on the relative location offsets between the jammer and the false point target. Therefore, this part can be generated in advance in implementing the jamming approach.

However, Part Π is closely related to the slow time (η) and the speed (v) of the SAR platform. Since the center slant range R_c between the jammer and the SAR platform can be calculated in advance with predicted platform flying track, it can be implied that the false scene can be stored before starting the jamming operation, thus rendering real-time implementation possible. Moreover, since the real-time generated delay signal is only related to the azimuth position x and the slow time η, we can sum Part I along the range to reduce the computational complexity and Part Π can accumulate the azimuth after the real time generation. In doing so, the delays of all targets in a false scene can be completed in one pulse repetition interval.

IV. SAR IMAGING PERFORMANCE UNDER FDA DECEPTIVE JAMMING

Without loss of generality, we employ the range-Doppler (RD) algorithm to evaluate the SAR imaging performance with the FDA deceptive jamming. The RD imaging algorithm consists of three steps: Range compression, range cell migration correction, and azimuth compression.

A. RANGE COMPRESSION

Applying Fourier transform to (10) with respect to the fast time t yields the representation of SAR returned signals in the range-frequency and azimuth-time domain:

$$\begin{aligned} S(f_r, \eta) &= \int_{-\infty}^{+\infty} s(t, \eta) \exp(-j2\pi f_r t)\, dt \\ &\approx \sum_{k=0}^{M-1} A_0 W_r(f_r)\, \omega_a(\eta - \eta_c) \exp\left(-j\frac{\pi f_r^2}{K_r}\right) \\ &\quad \times \exp\left\{-j\pi\left(\frac{(k\Delta f)^2}{K_r} + 4f_0\frac{R(\eta)}{c}\right)\right\} \\ &\quad \times \exp\left\{j2\pi\left(\frac{k\Delta f}{K_r} - \frac{2R(\eta)}{c}\right) f_r\right\} \end{aligned} \tag{13}$$

where $W_r(f_r) = \omega_r\left(f_r / K_r\right)$ is the range spectrum envelope.

With the reference function for range compression, (14) can be obtained:

$$h_r(t) = \omega_r(t) \exp\left(-j\pi K_r t^2\right) \tag{14}$$

After range compression, we can get the corresponding time-domain expression:

$$\begin{aligned} s(t, \eta) &= \mathrm{IFFT}_r\{S(f_r, \eta) H_r(f_r)\} \\ &= \sum_{k=0}^{M-1} A_0 \omega_a(\eta - \eta_c) \frac{B_r \sin \pi B_r\left(t + \frac{k\Delta f}{K_r} - \frac{2R(\eta)}{c}\right)}{\pi B_r\left(t + \frac{k\Delta f}{K_r} - \frac{2R(\eta)}{c}\right)} \\ &\quad \times \exp\left\{-j\pi\left(\frac{(k\Delta f)^2}{K_r} + 4f_0\frac{R(\eta)}{c}\right)\right\}. \end{aligned} \tag{15}$$

B. RANGE CELL MIGRATION CORRECTION AND AZIMUTH COMPRESSION

Applying Fourier transform to (15) with respect to the slow time η, we can get

$$\begin{aligned} S(f_r, f_\eta) &= \int_{-\infty}^{+\infty} s(t, \eta) \exp\left(-j2\pi f_\eta \eta\right) d\eta \\ &= \sum_{k=0}^{M-1} A_0 \exp\left\{j2\pi\left(\frac{k\Delta f}{K_r} - \frac{2R_c}{c}\right) f_r\right\} \\ &\quad \times \exp\left\{-j\pi\left(\frac{(k\Delta f)^2}{K_r} + 4f_0\frac{R_c}{c}\right)\right\} \\ &\quad \times W_a(f_\eta - f_{\eta_c}) \exp\left(j\pi\left(\frac{f_\eta^2}{K_a} - f_r\frac{cR_c f_\eta^2}{2v^2 f_0^2}\right)\right) \end{aligned} \tag{16}$$

where $K_a = \frac{2V_r^2}{\lambda_0 R_c}$ is the azimuthal frequency modulation rate, $V_r = v \sin\beta$ is the radial speed, β is the angle between the antenna phase center and the line of the point target and the vertical range of the beam, $W_a\left(f_\eta - f_{\eta_c}\right)$ is the frequency-domain representation of $\omega_a(\eta - \eta_c)$, and f_{η_c} is the Doppler center frequency. The azimuth compression function is

$$H_a\left(f_\eta\right) = \exp\left(-j\pi\frac{f_\eta^2}{K_a}\right). \tag{17}$$

$$s'(f_r, \eta) = A s(f_r, \eta) \left\{ \underbrace{\sum_y \sigma(x, y) \exp\left\{-j4\pi\left(\frac{f_r}{c} + \frac{1}{\lambda_0}\right)\left(y + \frac{x^2}{2R_c}\right)\right\}}_{Part\ I} \underbrace{\sum_x \exp\left\{j4\pi\frac{xv\eta}{R_c}\left(\frac{f_r}{c} + \frac{1}{\lambda_0}\right)\right\}}_{Part\ \Pi} \right\} \tag{12}$$

TABLE 1. Simulation parameters.

System Parameter	Numerical Value
Carrier Frequency	$15GHz$
Bandwidth	$100MHz$
Pulse Width	$40us$
Height of Transmitter	$3000m$
Incidence	45°
Pulse Repetition Frequency	$500Hz$
Aperture Length	$112m$
Platform Velocity	$100m/s$

The corresponding reference function for range cell migration correction is

$$H_{\mathrm{rmc}}(f_r) = \exp\left(j\pi f_r \frac{cR_c f_\eta^2}{2v^2 f_0^2}\right). \tag{18}$$

Therefore, after range cell migration correction and azimuth compression, we have

$$\begin{aligned} s(t,\eta) &= \mathrm{IFFT}_a\left\{S(f_r,f_\eta) H_a(f_\eta) H_{\mathrm{rmc}}(f_r)\right\} \\ &= \sum_{k=0}^{M-1} A_0 \exp\left(-j\pi \frac{(k\Delta f)^2}{K_r}\right) \exp\left(-j\frac{4\pi f_0 R_c}{c}\right) \\ &\quad \times \frac{B_r \sin\left(\pi B_r\left(t+\frac{k\Delta f}{K_r}-\frac{2R_c}{c}\right)\right)}{\pi B_r\left(t+\frac{k\Delta f}{K_r}-\frac{2R_c}{c}\right)} \frac{B_a \sin(\pi B_a \eta)}{\pi B_a \eta} \end{aligned} \tag{19}$$

where B_a is the Doppler bandwidth.

By observing (19), we can reach the following conclusions: Firstly, the jamming only poses impacts on the range-dimensional image. Secondly, the number of false targets is directly related to the number of FDA elements. Thirdly, the range between two false targets is determined by the $\frac{\Delta fc}{2K_r}$. Moreover, the positions of false targets can be controlled by designing the FDA parameters. In addition, if

$$\frac{\Delta f}{K_r} \cdot \frac{c}{2} \cdot \frac{2f_s}{c} = \Delta f 2\tau < 1 \tag{20}$$

where $f_s = 2B_r$, the SAR image will be defocused. Equation (20) also implies that the false target repeats itself at a period of $\Delta f 2\tau$ in the range dimension.

C. IMAGING SIMULATION RESULTS

Suppose the SAR operates at the side-looking mode, the synthetic aperture time is approximately $1.12s$, and the imaging area is 1 km $\times$1 km. Typical simulation parameters are listed in Table 1.

Firstly, we simulate the deceptive jamming against SAR in point-target imaging. Suppose the element numbers are set to 8 and 16 respectively. This frequency offset is set to $500kHz$. From the imaging simulation results given in Fig. 3, we can conclude that: Firstly, under the deceptive jamming, the SAR generates multiple false targets, which are evenly distributed in the range dimension, which can be seen from the comparison between Fig. 3(a) and Fig. 3(f), the proposed deceptive jamming method is verified here. Secondly, from Fig. 3(a) and Fig. 3(b), it can be seen that the number of false targets can be increased by increasing the array elements. Thirdly, if the frequency offset of each array is changed linearly, then the ranges between false targets are uniformly distributed, and the imaging intensity of false targets is the same, as shown in Fig. 3(e). If the frequency offsets are randomly distributed, the ranges between false targets are also random, as shown in Fig. 3(c). From Fig. 3(a), Fig. 3(c) and Fig. 3(d), the range distribution varies with the distribution of frequency offsets. For constant frequency deviation, we can change the range between false targets by controlling the pulse duration as shown in Fig. 3(e) and Fig. 3(a).

Next, we simulate the deceptive jamming against SAR in distributed-scene imaging. Suppose the simulation parameters: $\tau = 40\mu s$, $\Delta f = 4$ MHz, $M = 8$, and the jammed areas are 256×256 and 70×70 cells respectively. Fig. 4(a) is the jamming template of an airport with 256×256 cells. Fig. 4(b) is the airport runway to be jammed. Fig. 4(c) is the jamming result generated by the small jamming scene template. Compared to Fig.4(b), Fig.4(c) adds eight jamming airports and ranks the false surface targets in the range direction. Fig. 4(d) is the jamming effect of the large jamming scene template for the airport runway. Fig. 4(e) is the result with weighted frequency offsets, and Fig. 4(f) is the imaging result under four-element FDA deceptive jamming.

In order to control the appearance and disappearance of false scenes, we consider that the linear frequency offsets are multiplied by a weight vector $\overrightarrow{W}$

$$\overrightarrow{W} = \begin{bmatrix} 1 & 1 & 0 & 0 & 0 & 1 & 0 & 1 \end{bmatrix} \tag{21}$$

where 0 means that there are no jamming effects. As can be seen from Fig. 4(d), there are eight edges overlapped. Because the template range length is greater than the ranges between false targets. To avoid overlapped edges, we use the template with a small scene. Another way is to use the weighted frequency offset. The simulation results of these two approaches are shown in Fig. 4(c) and Fig. 4(e), respectively. It is observed from Fig. 4(d) and Fig. 4(e) that, the number and the location of false scenes can be changeable by controlling the weight vector $\overrightarrow{W}$. From Fig. 4(d) and Fig. 4(f), we can find that the jamming scene increases with the number of antenna array.

What follows is the simulation of the jamming effect on a moving target. Suppose the speed of the target is $10m/s$. The imaging simulation results of the moving target are shown in Fig. 5. Fig. 5(a) is a normal SAR image of the moving target and the phenomenon of the defocus is consistent with the theory. Fig. 5(b) is the imaging of the moving target with an FDA jammer. This indicates that the proposed method can also produce deceptive jamming effect on the moving targets.

V. DECEPTION JAMMING PERFORMANCE ANALYSIS

This section is a quantitative analysis of the jamming results. First, the imaging resolution and peak side-lobe ratio (PSLR) of the false point target and true point target are discussed.

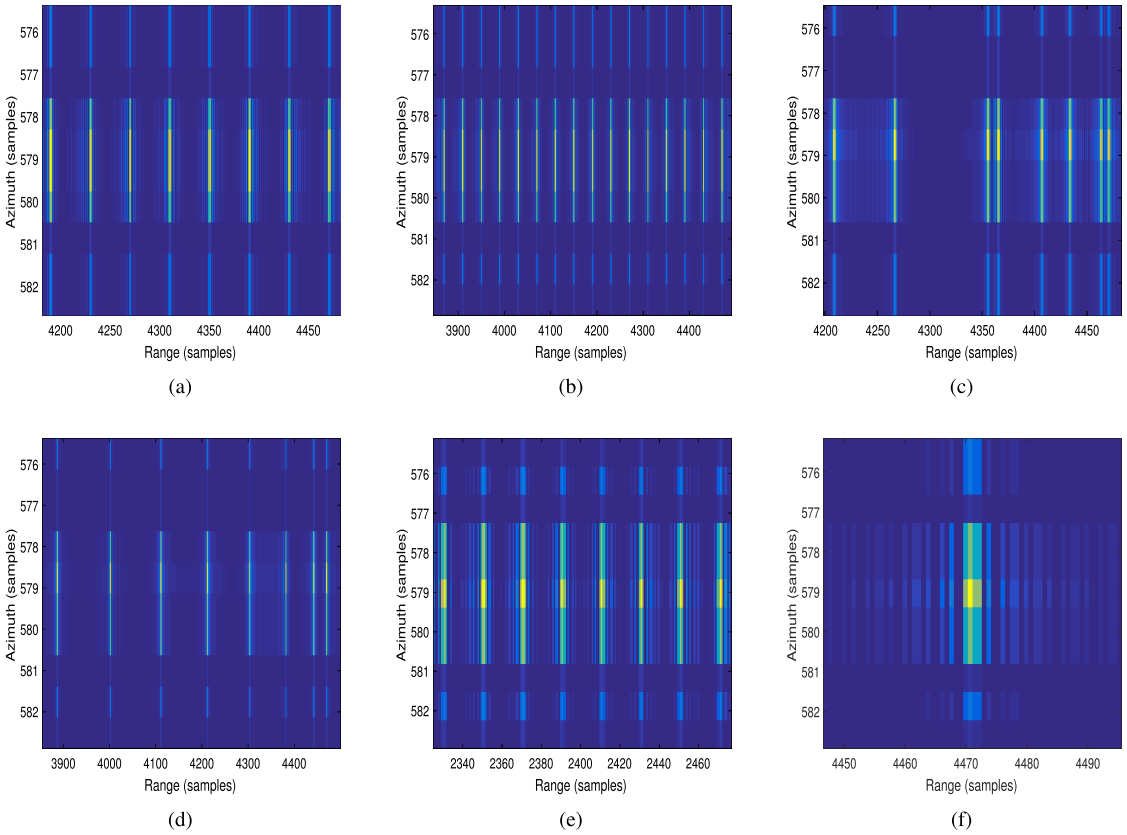

FIGURE 3. Deceptive jamming result of SAR imaging (a) Linear frequency offset (8 elements). (b) Linear frequency offset (16 elements). (c) Random frequency offset. (d) Exponential frequency offset. (e) Linear frequency offset ($\tau = 20us$). (f) Normal SAR imaging.

Then, we analyze the effect of frequency offset on imaging resolution and discuss the use of frequency offset and pulse width to control the range between false targets. Next, some statistics are given to evaluate the jamming effect of the scene. Finally, we analyze the computational complexity of deception scenarios generation.

A. IMAGING PERFORMANCE ANALYSIS

The peak side-lobe ratio is defined as the ratio of the maximum side-lobe peak (P_s) of the point target impulse response and the peak value of the main lobe (P_m) as shown in (22). This ratio determines the ability of the strong target to conceal the weak target.

$$\mathrm{PSLR} = 20\lg\left(\frac{P_s}{P_m}\right) \tag{22}$$

where PSLR_r and PSLR_a are respectively peak side-lobe ratio in the range and azimuth direction. Fig. 6(a) is the contour of the true point target, which indicates that the point target is well focused. Fig. 6(d) is the contour of the false point target from the jammer. From Fig. 6(b), we can see that PSLR_r is close to the theoretical value $-13.22dB$. Fig. 6(c) is the azimuth profile, with PSLR_a reaching $-13.25dB$. False point target resolution and peak side-lobe ratio generated by jammer is shown in Table 2, where the digital

TABLE 2. Imaging performance (the unit of resolution and PSLR is *m* and *dB*, respectively.)

	Range		Azimuth	
	Resolution	PSLR	Resolution	PSLR
true point target	1.34	−13.22	0.35	−13.25
1	1.5	−13.77	0.40	−13.24
2	1.5	−14.44	0.40	−13.32
3	1.5	−14.07	0.40	−13.36
4	1.5	−13.74	0.40	−13.41
5	1.5	−13.42	0.40	−13.44
6	1.5	−13.16	0.40	−13.48
7	1.5	−12.76	0.40	−13.54
8	1.5	−12.12	0.40	−13.61

1, 2, 3, 4, 5, 6, 7, 8 represent the false point targets produced by the FDA jammer respectively. From table 2 we can see that the resolution of each false point target hardly changes. The range of PSLR_a varies little. By observing PSLR_r and PSLR_a we can known that each false point target can be imaged perfectly. Because there are few differences between the PSLR of the true target and the false point targets produced by FDA, the jammer can pose effective jamming effect on SAR imaging system.

B. INFLUENCE OF FREQUENCY OFFSET

We analyze the effect of frequency offset on imaging resolution when other parameters remain the default value

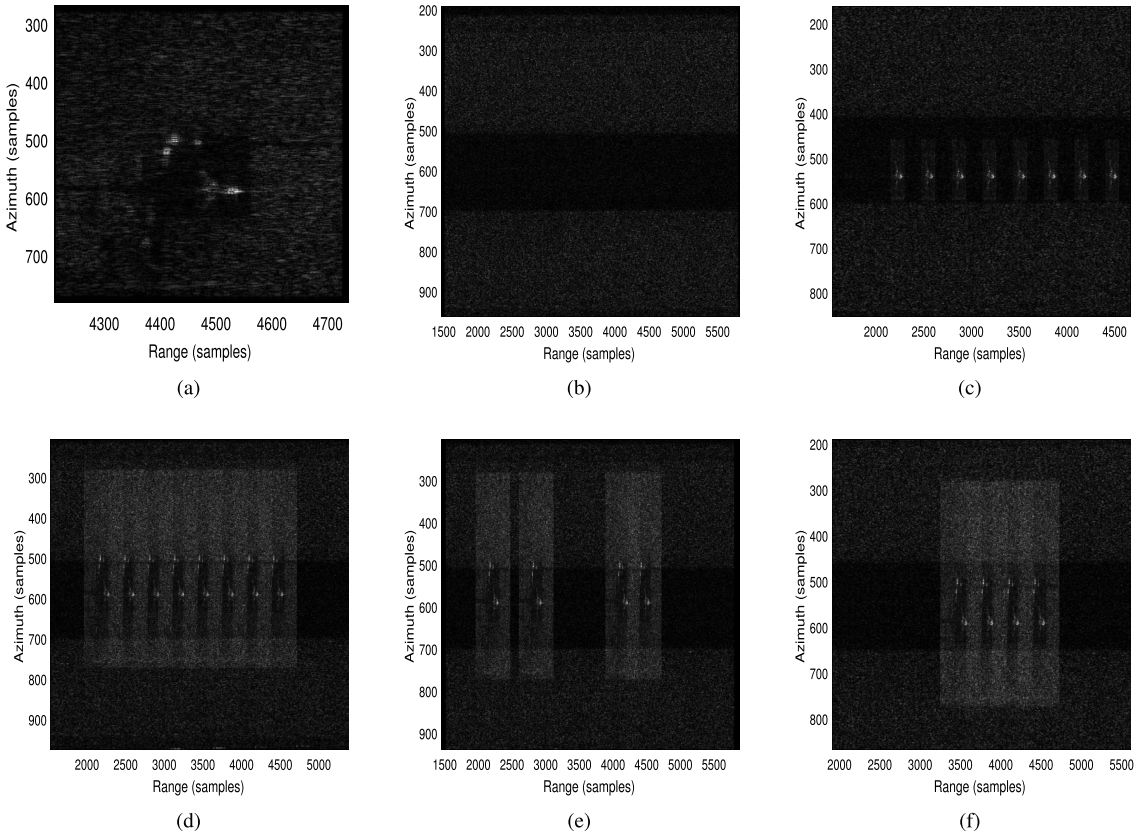

FIGURE 4. Scene imaging of deception jamming (a) Jamming scene template. (b) Airport runway. (c) Jamming imaging result (small scene). (d) Jamming imaging result (linear frequency offset). (e) Jamming imaging result (weighted frequency offset). (f) Jamming imaging result (4 elements).

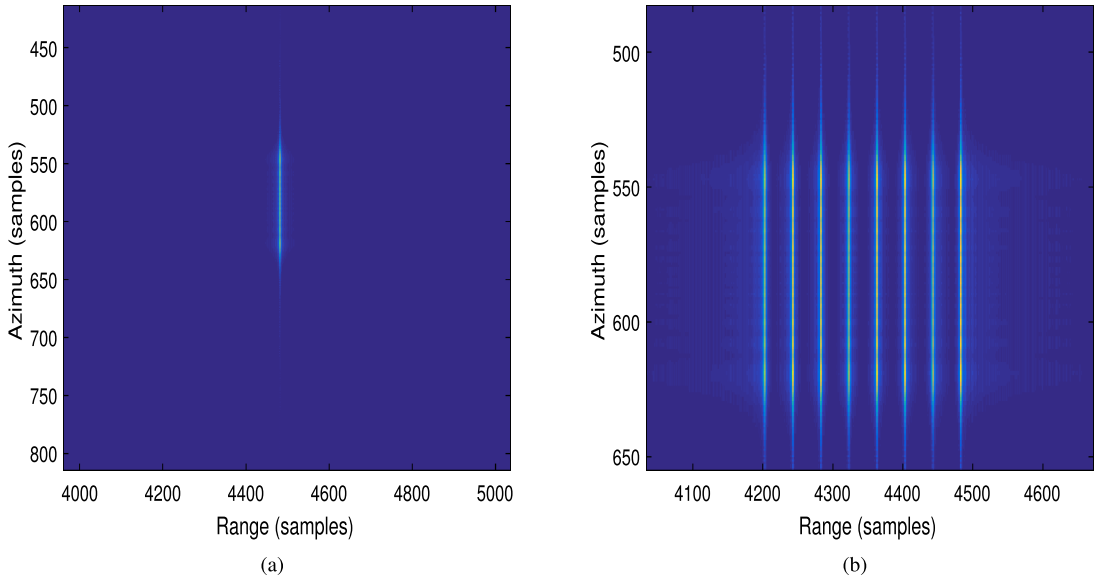

FIGURE 5. Moving target imaging result (a) Moving target imaging. (b) Moving target imaging with FDA jamming.

($\tau = 40us$). We can see from Fig.7 that when the frequency deviation is less than $250Hz$, the false target produced by the jammer can be imaged normally when between $2500Hz$ and $25KHz$, the phenomenon of defocus will appear in the SAR imagery and that when greater than $50KHz$, multiple false targets can appear in SAR imaging system. Therefore, the effective deception jamming performance can be obtained in the SAR system. When the frequency deviation is smaller,

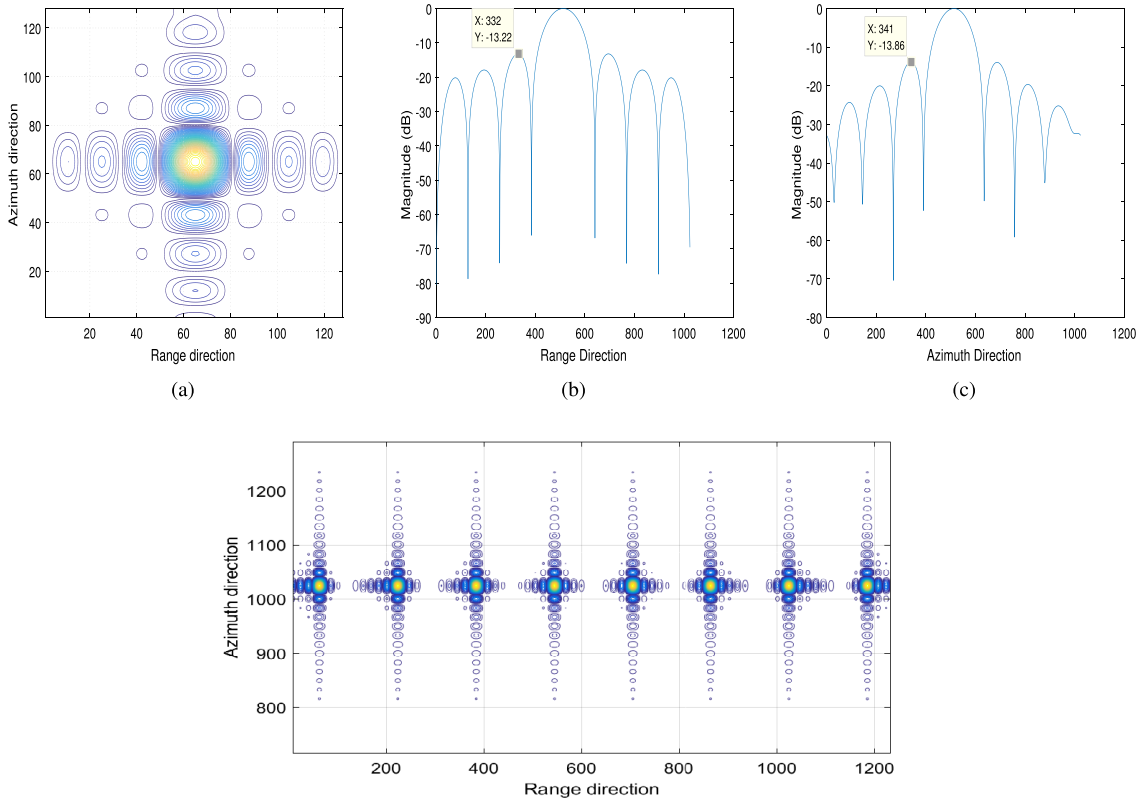

FIGURE 6. Compression characteristics of true target and false target: (a) True point target contour. (b) range profile. (c) azimuth profile. (d) FDA-based jamming contour.

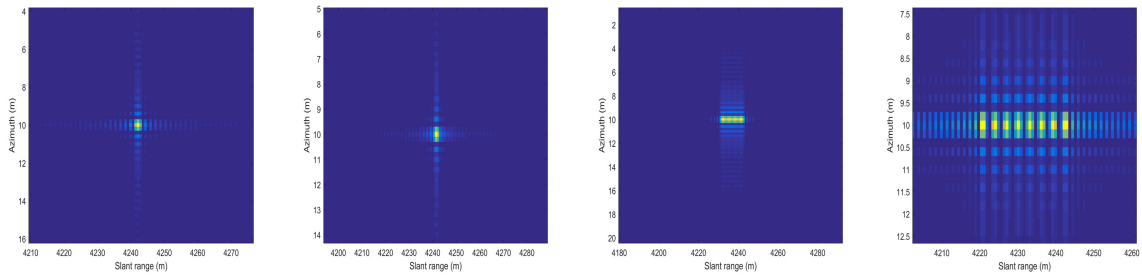

FIGURE 7. The effect of frequency offset on imaging: (a) $\Delta f = 250Hz$. (b) $\Delta f = 2500Hz$. (c) $\Delta f = 25KHz$. (d) $\Delta f = 50KHz$.

or the frequency offset is bigger, we define the range between false targets as follows:

$$R_{\mathrm{FT}} = \Delta f \, \tau \frac{c}{2B_r}. \tag{23}$$

Here, we only discuss the effect of frequency offsets and pulse width on the range between false targets. From Fig. 7 and Fig. 8, we can see that by increasing the pulse width or the frequency offset, the range between false point targets also increase. Generally speaking, the pulse width of the jammer is determined by the other radar. Therefore, the range between the false target can be controlled by changing the frequency offset. However, the frequency offset must be controlled within a certain range.

C. STATISTICAL ANALYSIS

The mean value of the image is the average intensity of the image, which reflects the average gray level of the image, i.e. the average backscattering coefficient of the target contained in the image. The variance of the image represents the degree of deviation from the mean of all pixels in the image region, which reflects the uniformity of the image. Assuming the image size is $N \times M$, the mean (μ) and variance (σ^2) can

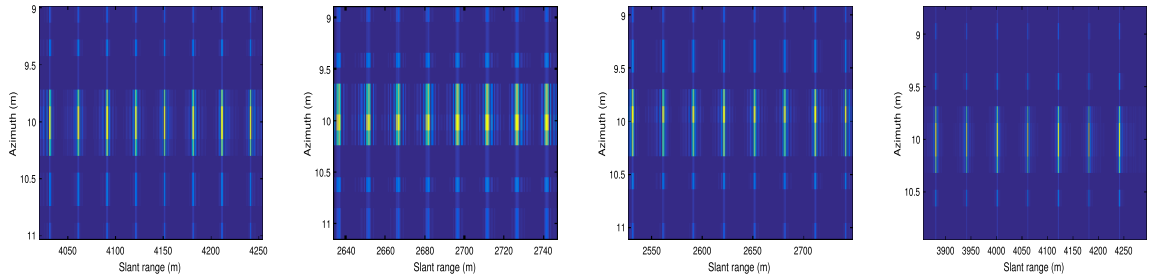

FIGURE 8. Range between false targets: (a) $\Delta f = 500KHz$, $\tau = 40us$. (b) $\Delta f = 500KHz$, $\tau = 20us$. (c) $\Delta f = 1MHz$, $\tau = 20us$. (d) $\Delta f = 1MHz$, $\tau = 40us$.

be written separately as:

$$\mu = \frac{1}{NM}\sum_{i=1}^{N}\sum_{j=1}^{M} I_{ij} \tag{24}$$

$$\sigma^2 = \frac{1}{NM}\sum_{i=1}^{N}\sum_{j=1}^{M} \left(I_{ij} - \mu\right)^2 \tag{25}$$

where I_{ij} is the value of the SAR image at the (i, j) point. The mean and variance of image is the index to reflect the whole feature of image. Under normal circumstances, if the topography, vegetation is different, then there will be different backscattering coefficients, reflected in the SAR image that has different image mean values and variances. In the image scene, the terrain difference is big, the artificial targets are many, the image gray value change is bigger, the image variance is also bigger. Generally speaking, deception jamming is a strong point target in the scene. Therefore, the mean and variance of the image will be changed.

The equivalent number of looks (ENL) is an indicator commonly used in image evaluation, which represents the contrast of image gray scale. Its expression is as follows:

$$\mathrm{ENL} = \frac{\mu^2}{\sigma^2} \tag{26}$$

The larger the ENL is, the smaller the contrast of image is, the more blurred the image becomes. Hence, ENL can effectively measure the jamming effect of SAR. Equation (27) can indicate the extent of the image being disturbed.

$$\Delta\mathrm{ENL} = \frac{\mathrm{ENL}_s}{\mathrm{ENL}_J} \tag{27}$$

where ENL_s is the ENL of the original image, ENL_J is the ENL of the jamming image. The greater the degree of ENL is away from 1, the greater the degree of interference of SAR gets, the better the jamming effect becomes. On the contrary, the smaller the degree of SAR interference, the worse the jamming effect.

We assume that $H(x)$ represents the average uncertainty of the original SAR image, and $H(x|y)$ represents the mean uncertainty of the jamming SAR image, then the amount of information obtained from the jamming SAR image is a priori uncertainty minus the uncertainty (determined by the superposition of disturbances and signals), it can be written as:

$$\Delta H\left(x\right) = H\left(x\right) - H\left(x|y\right) \tag{28}$$

For the same target scene and the same imaging algorithm, by calculating and comparing the changes of $\Delta H(x)$, we can evaluate the effectiveness of jamming or compare the quality of different jamming styles. The greater the $\Delta H(x)$ indicates that the more information is lost in the SAR image after jamming, the worse the image becomes, the better the jamming effect is.

$$H\left(x\right) = -\sum_{m=1}^{M}\sum_{n=1}^{N} p_{m,n}\log\left(p_{m,n}\right) \tag{29}$$

$$p_{m,n} = \frac{I_{m,n}^2}{\sum_{i=1}^{M}\sum_{j=1}^{N} I_{i,j}^2} \tag{30}$$

where $H(x|y)$ and $H(x)$ solution methods are primarily the same. $I_{m,n}$ represents the image strength at the pixel position (m, n).

Wang and others put forward a method of image quality evaluation based on the structural similarity (SSIM) [36], the basic idea of which runs that the main function of the human beings' vision system is to extract the structural information from the visual region, compare the similarity of two images, rather than the difference, and obtain the image of similar structure, so as to obtain the objective predictive quality. SSIM divides the image into three groups according to the brightness, contrast, structure, respectively, and then the weighted product to obtain the similarity. SSIM can be used to evaluate the anti-jamming capability of SAR. Its mathematical expression is as follows:

$$\mathrm{SSIM}\left(x, y\right) = \left[l\left(x, y\right)\right]^{\alpha}\left[c\left(x, y\right)\right]^{\beta}\left[s\left(x, y\right)\right]^{\gamma} \tag{31}$$

TABLE 3. Statistical feature.

	Fig.4(b)	Fig.4(c)	Fig.4(d)	Fig.4(e)
Mean	5.8	21.89	18.79	20.24
Variance	16.83	1.6×10^4	4.3×10^6	2.0×10^5
ΔENL	×	1.5×10^{-2}	4.0×10^{-5}	1.2×10^{-3}
SSIM	×	0.45	0.80	0.59
ΔH	×	1.03	0.67	1.28

where x and y represent the SAR original image and the image after the jamming respectively. The α, β, γ are weighted indices respectively.

$$l(x,y) = \frac{2\mu_x\mu_y + C_1}{\mu_x^2 + \mu_y^2 + C_1}$$
$$c(x,y) = \frac{2\sigma_x\sigma_y + C_2}{\sigma_x^2 + \sigma_y^2 + C_2}$$
$$s(x,y) = \frac{\sigma_{x,y} + C_3}{\sigma_x\sigma_y + C_3} \tag{32}$$

where $l(x,y)$, $c(x,y)$, $s(x,y)$ respectively, represent brightness, contrast, and structural factors, which can be used to measure to what extent the SAR images are disturbed. μ_x, μ_y are the pixel gray mean value of the original image and the jamming image respectively, which characterizes the brightness of the image. σ_x, σ_y are the standard deviation of pixel gray scale in original image and jamming image respectively, characterized by the contrast of images. $\sigma_{x,y}$ is the correlation coefficient between the original image and the jamming image corresponding block, and the similarity of the structure information is represented. C_1, C_2, and C_3 are small positive numbers that avoid the denominator being zero or nearly 0.

The higher the SSIM value, the lower the degree of interference in the quality of the SAR image, and the result will be affected by selecting a different size of the child block. From the above analysis, SSIM is the measurement of the distortion degree of the spatial SAR image structure information.Statistical characteristics before and after interference are shown in Table 3.

Where × doesn't make sense to represent this parameter. Fig. 4(b) represents the undisturbed original scene. Fig. 4(c), Fig. 4(d), Fig. 4(e) represent a scene that is disturbed by different methods. From the first and second rows of table 3, we can see that the mean and variance of the disturbed image are larger, indicating that this parameter can be used to evaluate the jamming effect. From the previous theoretical analysis, it can be learned that ΔENL is far less than 1 and can produce a good interference effect. The ΔENL value of the image after jamming is in accordance with theoretical analysis. It can be seen from table 3 that the SSIM value after interference is very small, indicating that the interference effect of the image is very good. The value of ΔH is greater than 0, indicating that the image is disturbed. From table 3, the above statistics can be used to quantitatively evaluate the jamming effect.

D. COMPUTATIONAL COMPLEXITY OF JAMMING SIGNALS GENERATION

Suppose the data sampling point in a PRT is L, and scene size is $M \times N$. $4\pi\left(\frac{f_r}{c} + \frac{1}{\lambda_0}\right)$ can be calculated as a constant in advance. The exponential term of Part I requires 3 times real multiplication operation and once real addition operation. The exponential term of Part II requires 4 times real multiplication operation. $\sigma(x,y)$ is a complex data. Part I need ML times complex multiplication and $M(L-1)$ times complex addition operations. ML times complex multiplication can be decomposed into $4ML$ times real multiplication $2ML$ times real addition. Therefore, Part I and Part II need MNL times complex multiplication and $ML(N-1)$ times complex addition operation altogether. In a PRT, the total computational complexity of the deception signal is made up of $48MNL$ times real multiplication and $2M(LN-1)+1$ times addition.

VI. CONCLUSION

Deceptive jamming on SAR with FDA was proposed in this paper. Multiple false targets or scenes can be evenly placed in the final SAR imaging system, and false scenes increase as the number of arrays increases. The range between false scenes can be controlled by changing the frequency offset. The appearance and disappearance of false scenes are controlled by weight vectors. Simulation results verify that the proposed method can exert effective deception jamming effect on SAR imaging system, whether it is a static target or scene or a moving target. It should be noted that this paper only designs deception jamming algorithm for side-looking SAR imaging. In the near future, we will further study deception jamming methods for squint SAR and spaceborne SAR imaging.

APPENDIX
TAYLOR EXPANSION

This appendix will analyze the effect of the Taylor expansion on performance of phase error. Using Taylor to expand. Equation (2) can be written as:

$$\begin{aligned} R(\eta) &= \sqrt{R_s^2 + h^2 + (v\eta)^2} = \sqrt{R_s^2 + h^2}\sqrt{1 + \frac{(v\eta)^2}{\left(R_s^2 + h^2\right)}} \\ &\approx \sqrt{R_s^2 + h^2}\left(1 + \frac{(v\eta)^2}{2\left(R_s^2 + h^2\right)} - \frac{1}{8}\left(\frac{(v\eta)^2}{R_s^2 + h^2}\right)^2\right) \\ &\approx R_s + \frac{h^2}{2R_s} + \frac{(v\eta)^2}{2R_c} - \frac{1}{8}\frac{(v\eta)^4}{\left(R_s^2 + h^2\right)^{3/2}} \end{aligned} \tag{A1}$$

If the phase error is smaller than $\pi/12$, then its influence is ignorable.

$$\frac{4\pi}{\lambda}\frac{1}{8}\frac{(v\eta)^4}{\left(R_s^2 + h^2\right)^{3/2}} < \frac{\pi}{12} \tag{A2}$$

This equation (A2) is usually satisfied in the side-looking SAR imaging. So, the fourth item of the equation (A1) can be ignored.

REFERENCES

[1] F. Gao, F. Ma, J. Wang, J. Sun, E. Yang, and H. Zhou, "Visual saliency modeling for river detection in high–resolution SAR imagery," *IEEE Access*, vol. 6, pp. 1000–1014, 2018.
[2] W. Lv, K. Dai, L. Wu, X. Yang, and W. Xu, "Runway detection in SAR images based on fusion sparse representation and semantic spatial matching," *IEEE Access*, vol. 6, pp. 27984–27992, 2018.
[3] S. Brusch, S. Lehner, T. Fritz, M. Soccorsi, A. Soloviev, and B. Van Schie, "Ship surveillance with TerraSAR–X," *IEEE Trans. Geosci. Remote Sens.*, vol. 49, no. 3, pp. 1092–1103, Mar. 2011.
[4] J. Chen, B. Zhang, and C. Wang, "Backscattering feature analysis and recognition of civilian aircraft in TerraSAR–X images," *IEEE Geosci. Remote Sens. Lett.*, vol. 12, no. 4, pp. 796–800, Apr. 2015.
[5] J. Xu, B. Bai, C. Dong, and G. Zhao, "A novel passive jamming method against ISAR based on resonance absorption effect of metamaterials," *IEEE Access*, vol. 6, pp. 18142–18148, 2018.
[6] R. Wang, X. Wang, S. Cheng, Y. Meng, G. Zhang, and Y. Zhou, "Plasma passive jamming for SAR based on the resonant absorption effect," *IEEE Trans. Plasma Sci.*, vol. 46, no. 4, pp. 928–933, Apr. 2018.
[7] J. Xu, B. Bai, C. Dong, Y. Zhu, Y.-Y. Dong, and G. Zhao, "A novel plasma jamming technology based on the resonance absorption effect," *IEEE Antennas Wireless Propag. Lett.*, vol. 16, pp. 1056–1059, 2017.
[8] S. Joy, L. H. Nguyen, and T. D. Tran, "Radio frequency interference suppression in ultra-wideband synthetic aperture radar using range-azimuth sparse and low-rank model," in *Proc. IEEE Radar Conf. (RadarConf)*, May 2016, pp. 1–4.
[9] L. Fang and W. J. Guo, "Analysis of barrage-type jamming J/S isosurface to bistatic SAR," in *Proc. 2nd Asian–Pacific Conf. Synth. Aperture Radar*, Oct. 2009, pp. 848–851.
[10] W. Xiang, J. Wang, and F. Liu, "The exposed area analysis of Barrage-type jamming to bistatic SAR," in *Proc. Int. Conf. Electron. Inf. Eng.*, vol. 2, 2010, pp. V2-168–V2-171.
[11] I. Goodfellow, J. Pouget-Abadie, M. Mirza, B. Xu, D. Warde-Farley, S. Ozair, A. Courville, and Y. Bengio, "Generative adversarial nets," in *Proc. Adv. Neural Inf. Process. Syst.*, 2014, pp. 2672–2680.
[12] Q. Liu, S. Xing, X. Wang, J. Dong, D. Dai, and Y. Li, "The interferometry phase of insar coherent jamming with arbitrary waveform modulation," *Prog. Electromagn. Res.*, vol. 124, pp. 101–118, 2012.
[13] Q. Shi, C. Wang, J. Huang, and N. Yuan, "Multiple targets deception jamming against ISAR based on periodic 0-π phase modulation," *IEEE Access*, vol. 6, pp. 3539–3548, 2018.
[14] X. He, J. Zhu, J. Wang, D. Du, and B. Tang, "False target deceptive jamming for countering missile–borne SAR," in *Proc. IEEE 17th Int. Conf. Comput. Sci. Eng.*, Dec. 2014, pp. 1974–1978.
[15] W. Wang and J. Cai, "A technique for jamming Bi- and multistatic SAR systems," *IEEE Geosci. Remote Sens. Lett.*, vol. 4, no. 1, pp. 80–82, Jan. 2007.
[16] C. Dong and X. Chang, "A novel scattered wave deception jamming against three channel SAR GMTI," *IEEE Access*, vol. 6, pp. 53882–53889, 2018.
[17] F. Zhou, B. Zhao, M. Tao, X. Bai, B. Chen, and G. Sun, "A large scene deceptive jamming method for space–borne SAR," *IEEE Trans. Geosci. Remote Sens.*, vol. 51, no. 8, pp. 4486–4495, Aug. 2013.
[18] Q. Sun, T. Shu, S. Zhou, B. Tang, and W. Yu, "A novel jamming signal generation method for deceptive SAR jammer," in *Proc. IEEE Radar Conf.*, May 2014, pp. 1174–1178.
[19] S. Long, Z. Hong-Rong, T. Yue-Sheng, and Z. Chang-Yao, "Research on deceptive jamming technologies against SAR," in *Proc. 2nd Asian–Pacific Conf. Synth. Aperture Radar*, Oct. 2009, pp. 521–525.
[20] B. Zhao, L. Huang, J. Li, M. Liu, and J. Wang, "Deceptive SAR jamming based on 1-bit sampling and time–varying thresholds," *IEEE J. Sel. Topics Appl. Earth Observ. Remote Sens.*, vol. 11, no. 3, pp. 939–950, Mar. 2018.
[21] B. Zhao, F. Zhou, and Z. Bao, "Deception jamming for squint SAR based on multiple receivers," *IEEE J. Sel. Topics Appl. Earth Observ. Remote Sens.*, vol. 8, no. 8, pp. 3988–3998, Aug. 2015.
[22] B. Zhao, L. Huang, F. Zhou, and J. Zhang, "Performance improvement of deception jamming against SAR based on minimum condition number," *IEEE J. Sel. Topics Appl. Earth Observ. Remote Sens.*, vol. 10, no. 3, pp. 1039–1055, Mar. 2017.
[23] D. Feng, L. Xu, X. Pan, and X. Wang, "Jamming wideband radar using interrupted–sampling repeater," *IEEE Trans. Aerosp. Electron. Syst.*, vol. 53, no. 3, pp. 1341–1354, Jun. 2017.
[24] Y. Liu, W. Wang, X. Pan, L. Xu, and G. Wang, "Influence of estimate error of radar kinematic parameter on deceptive jamming against SAR," *IEEE Sensors J.*, vol. 16, no. 15, pp. 5904–5911, Aug. 2016.
[25] Y. Liu, D. Feng, X. Pan, D. Dai, and W. Wang, "A frequency-domain three-stage algorithm for active deception jamming against synthetic aperture radar," *IET Radar, Sonar Navigat.*, vol. 8, no. 6, pp. 639–646, Jul. 2014.
[26] J. Zhang, D. Zhu, and G. Zhang, "New antivelocity deception jamming technique using pulses with adaptive initial phases," *IEEE Trans. Aerosp. Electron. Syst.*, vol. 49, no. 2, pp. 1290–1300, Apr. 2013.
[27] S. Xu, J. Liu, Y. Li, and Y. Fu, "A new deceptive jamming method for SAR based on false moving targets," in *Proc. Int. Conf. Radar*, Sep. 2008, pp. 371–374.
[28] Y. Liu, S. Gong, and X. Wei, "Deceptive moving targets jamming to SAR based on airborne platform," in *Proc. IEEE 11th Int. Conf. Signal Process.*, vol. 3, Oct. 2012, pp. 1905–1909.
[29] X. Li, D. Wang, X. Ma, and W.-Q. Wang, "FDS–MIMO radar low–altitude beam coverage performance analysis and optimization," *IEEE Trans. Signal Process.*, vol. 66, no. 9, pp. 2494–2506, May 2018.
[30] W.-Q. Wang, H. C. So, and A. Farina, "An overview on time/frequency modulated array processing," *IEEE J. Sel. Topics Signal Process.*, vol. 11, no. 2, pp. 228–246, Mar. 2017.
[31] R. Gui, W.-Q. Wang, C. Cui, and H. C. So, "Coherent pulsed–FDA radar receiver design with time–variance consideration: SINR and CRB analysis," *IEEE Trans. Signal Process.*, vol. 66, no. 1, pp. 200–214, Jan. 2018.
[32] P. F. Sammartino, C. J. Baker, and H. D. Griffiths, "Frequency diverse MIMO techniques for radar," *IEEE Trans. Aerosp. Electron. Syst.*, vol. 49, no. 1, pp. 201–222, Jan. 2013.
[33] W.-Q. Wang, "Cognitive frequency diverse array radar with situational awareness," *IET Radar, Sonar Navigat.*, vol. 10, no. 2, pp. 359–369, Feb. 2016.
[34] Y. Zhu, H. Wang, S. Zhang, Z. Zheng, and W. Wang, "Deceptive jamming on space–borne SAR using frequency diverse array," in *Proc. IEEE Int. Geosci. Remote Sens. Symp. (IGARSS)*, Jul. 2018, pp. 605–608.
[35] B. Huang, W.-Q. Wang, S. Zhang, H. Wang, R. Gui, and Z. Lu, "A novel approach for spaceborne SAR scattered-wave deception jamming using frequency diverse array," *IEEE Geosci. Remote Sens. Lett.*, to be published.
[36] Z. Wang, A. Bovik, H. Sheikh, and E. Simoncelli, "Image quality assessment: From error visibility to structural similarity," *IEEE Trans. Image Process.*, vol. 13, no. 4, pp. 600–612, Apr. 2004.

HUI WANG was born in Anhui, China, in 1992. He received the B.S. degree in electronic and information engineering from the Chengnan College, Changsha University of Science and Technology, Changsha, China, in 2015, and the M.E. degree in electronics and communication engineering from the University of Electronic Science and Technology of China (UESTC), Chengdu, China.

He holds one patent. He has published three international conference papers. His research interests include radar signal processing and radar imaging, SAR imaging of high-precision, and SAR jamming using frequency diverse array (FDA).

SHUNSHENG ZHANG was born in Anhui, China, in 1980. He received the Ph.D. degree in signal and information processing from the Beijing Institute of Technology, Beijing, China, in 2007.

In October 2007, he joined the Research Institute of Electronic Science and Technology, University of Electronic Science and Technology of China, Chengdu, China. In August 2009, he became an Associate Professor with the University of Electronic Science and Technology of China. From May 2014 to May 2015, he was a Visiting Scholar with the Department of Electrical and Computer Engineering, National University of Singapore. His major research interests include radar imaging (SAR/ISAR) and the application of frequency diverse array technology.

WEN-QIN WANG (Senior Member, IEEE) received the B.E. degree in electrical engineering from Shandong University, Shandong, China, in 2002, and the M.E. and Ph.D. degrees in information and communication engineering from the University of Electronic Science and Technology of China (UESTC), Chengdu, China, in 2005 and 2010, respectively. From March 2005 to 2007, he was with the National Key Laboratory of Microwave Imaging Technology, Chinese Academy of Sciences, Beijing, China. Since September 2007, he has been with the School of Information and Communication Engineering, UESTC, where he is currently a Professor and the Director. From June 2011 to May 2012, he was a Visiting Scholar with the Stevens Institute of Technology, Hoboken, NJ, USA. From December 2012 to December 2013, he was a Hong Kong Scholar with the City University of Hong Kong, Hong Kong. From January 2014 to January 2016, he was a Marie Curie Fellow of Imperial College London, U.K. His research interests include array signal processing and circuit systems for radars, communication, and microwave remote sensing.

BANG HUANG was born in Hubei, China, in 1994. He received the B.E. degree from the School of Communication and Information Engineering, Chongqing University of Posts and Telecommunications, Chongqing, China, in 2017. He is currently pursuing the M.E. degree in electronic and communication engineering with the University of Electronic Science and Technology of China (UESTC), Chengdu, China.

His research interests include the SAR imaging of high-precision and SAR jamming using frequency diverse array (FDA).

ZHI ZHENG (Member, IEEE) received the M.S. and Ph.D. degrees in electronic engineering and information and communication engineering from the University of Electronic Science and Technology of China (UESTC), Chengdu, China, in 2007 and 2011, respectively. From 2014 to 2015, he was an Academic Visitor with the Department of Electrical and Electronic Engineering, Imperial College London, U.K. Since 2011, he has been with the School of Information and Communication Engineering, UESTC, where he is currently an Associate Professor. His research interests include statistical and array signal processing, including direction finding, source localization, target tracking, sparse array design, robust adaptive beamforming, jammer suppression, compressive sensing, machine learning, and convex optimization, with applications to radars, sonars, satellite navigation, wireless communications, and wireless sensor networks.

ZHENG LU (Senior Member, IEEE) received the B.S. degree in information engineering and the Ph.D. degree in target detection and recognition from the Beijing Institute of Technology, Beijing, China, in 2008 and 2013, respectively. He is currently a Senior Engineer with the Beijing Institute of Spacecraft System Engineering, China Academy of Space Technology (CAST). He is also a Program Manager of the Spaceborne Bistatic SAR Team. He has published two academic books, more than 50 refereed journals articles and conference papers, and granted four and filed 11 national invention patents of China. His research interests include spaceborne radar systems and signal processing (particularly synthetic aperture radar and pulse Doppler radar). In these research fields, he is also a Principal Investigator and important participant of more than 15 grants and funding from different National or Governmental sources, including the National Natural Science Foundation of China (NSFC), the Management Office of Major Project of High-Resolution Earth Observation System, and the Department of Space Systems CAST Science and Technology Committee. He has received several awards and prizes, including the First Prize of National Surveying-Mapping Science and Technology Progress Award, in 2019, and the Distinguished Young Scholars Fund of CAST, in 2018.